BİTLİS EREN ÜNİVERSİTESİ
FEN BİLİMLERİ DERGİSİ

ISSN: 2147-3129 / e-ISSN: 2147-3188

Article Type	: Research Article	**Year**	: 2025
Received	: August 28, 2025	**Volume**	: 14
Revised	: December 20, 2025	**Issue**	: 4
Accepted	: December 21, 2025	**Pages**	: 2664-2683
DOI	: 10.17798/bitlisfen.1773151		

DETECTION AND COMPARATIVE ANALYSIS OF MUCILAGE FROM SATELLITE IMAGES USING DEEP LEARNING METHODS

Yunus Emre ÇUKUR [1], **Ertürk ERDAĞI [1,*]**

[1] *Istanbul Medeniyet University, Department of Computer Engineering, İstanbul, Türkiye*

**** Corresponding Author:*** *erturkerdagi@gmail.com*

ABSTRACT

Mucilage is an environmental problem that threatens biodiversity in marine ecosystems and poses socio-economic risks. In heavily polluted areas like the Marmara Sea, early detection of mucilage is crucial for maintaining ecological balance. Early detection allows policymakers to take swift action. This study utilizes deep learning methods to detect marine mucilage using satellite imagery. The study employed YOLOv7, YOLOv8, YOLOv11, and YOLOv12 models, along with transformer-based RF-DETR and Roboflow 3.0 architectures. A dataset comprising 1113 images from various satellite sources, with mucilage regions marked with bounding boxes, was used. The dataset was expanded using data enhancement techniques. The training process was improved by applying hyperparameters to all models, resulting in performance gains. The performance of the models used in the study was evaluated using precision, recall, mAP@0.5, and mAP@0.5:0.95 metrics. Experimental results show that the YOLOv8 model achieved higher success rates than other methods. Hyperparameter settings were found to significantly impact model performance. Evaluations indicate difficulties in mucilage detection due to low-resolution images and image complexity in coastal areas. This study demonstrates the applicability of artificial intelligence technologies for monitoring environmental problems and provides a decision-support infrastructure for early-warning systems.

Keywords: Mucilage, Sea, YOLO, Deep learning, Satellite imagery, mAP.

1 INTRODUCTION

Mucilage is a sticky biological formation with a gelatinous structure composed of organic matter, bacteria, and microalgae found in the marine ecosystem [1]. This structure is generally formed in semi-enclosed or enclosed seas due to low current circulation, rising sea

temperatures, and high nutrient loads [2]. Increased levels of elements such as nitrogen and phosphorus are critical for mucilage formation. These increases are caused by excessive fertilizer use in agriculture, industrial waste, and household sewage carried into the sea [3].

The first report on mucilage was compiled for the Adriatic Sea in the 18th century [4]. Türkiye, located in the transition zone of the Sea of Marmara, has become the most vulnerable region due to its population density, industrial pollution, and limited water renewal. The formation of mucilage in the Sea of Marmara in 2021 caused significant problems in both quantity and duration, and the widespread mucilage has become a major issue on the country's agenda [5].

Mucilage has a permanent negative impact on the marine ecosystem. The dense mucilage layer forms on the sea surface, preventing sunlight from reaching the bottom [6]. Due to the sticky nature of mucilage, it can cause death by adhering to all parts of marine organisms or their gills [7]. The significant, long-term mucilage problem in the Sea of Marmara in 2021 affected fishing activities and negatively impacted marine tourism [8].

Mucilage is a factor affecting not only the marine ecosystem but also all vital activities. The decomposition of organic matter and bacterial activity in the sea facilitate the spread of pathogens, posing risks to human health. Therefore, mucilage should be considered not only as a biological element affecting the marine ecosystem but also as an environmental problem with socio-economic implications.

Methods for detecting and monitoring mucilage have evolved with technological advances. In traditional methods, researchers collected water samples from the sea and conducted various analyses in laboratory settings. This process enabled the determination of the structural form of the mucilage. However, this method has been limited by time, cost, and reliance on the workforce [9]. In recent years, observation reports have been prepared regarding the occurrence of mucilage on the sea surface. These reports are subjective because they are made by fishermen or members of the public working at sea. Therefore, it is essential to develop a more objective detection method for mucilage.

Significant advances have been made in monitoring marine research thanks to the development of satellite technologies. The capabilities of different satellite types enable monitoring of environmental changes [10]. Short-wave infrared structures observed on satellites can be used to determine the physical and biological properties of water. These structures are frequently used to detect oil spills, algal blooms, and other anomalies on the sea

surface. The Normalized Difference Chlorophyll Index (NDCI) and Floating Algae Index (FAI) structures can be used to estimate chlorophyll-a concentration in the sea [11]. However, due to the heterogeneous structure of mucilage and its similarity to other biological entities, these structures are not always sufficient to distinguish it. At this point, artificial intelligence technologies such as image processing, deep learning, and machine learning can be used to detect mucilage.

Deep learning has achieved high success in image studies thanks to the Convolutional Neural Network (CNN) model. Methods such as YOLO [12] and Faster R-CNN [13] can also be used for image-specific studies such as object detection, classification, and segmentation. In recent years, transformer-based approaches such as RF-DETR [14], Vision Transformer [13] have gained prominence due to their ability to model long-range dependencies. Deep learning models can be used to detect forest fires, classify marine litter, and estimate algae abundance [15]. This method also allows for automatic detection of mucilage using satellite imagery.

This study compares the performance of different deep learning models for mucilage detection. The YOLO architecture was chosen for this study due to its high success rate in real-time object detection and its speed-accuracy balance across four models. The RF-DETR architecture, which is not CNN-based and uses an attention mechanism, was used to test complex sea surface images. Roboflow models were specifically chosen because of their ease of labeling and their ability to transform image data in a way that can be used by machine learning and deep learning models. Hyperparameter optimization was performed in the study to improve performance. The results obtained demonstrate the usability of deep learning methods for detecting critical situations, such as mucilage.

2 LITERATURE REVIEW

Since the 1980s, mucilage events reported in the Central and Eastern Mediterranean Sea have shown that seawater warming, reduced circulation, and elevated marine biogenic elements have increased due to climate change [16]. The prolonged and widespread mucilage outbreak in the Sea of Marmara in 2021 caused losses in fishing and a contraction in tourism. Therefore, the establishment of monitoring and early warning systems has become crucial [17].

Remote sensing-based studies for the Sea of Marmara have monitored daily and seasonal changes in mucilage using the medium-range sensor MODIS and various indicators [18]. Detection and monitoring were conducted regionally and in some coastal areas using 10-

30 m resolution sensors such as Sentinel-2 and Landsat-8/9 [19]. Studies conducted after the 2021 event have addressed both the development and distribution of mucilage in the Sea of Marmara in a supportive manner, using data obtained from various perspectives. The results obtained showed that preprocessing and index selection are essential due to increased reflectance in optical bands and limited discrimination [20].

Analysis of mucilage spectral properties showed that it is mostly spectrally featureless, with a monotonic increase across the blue-red spectrum. Therefore, it has been observed that algorithms implemented using classical sea- and ocean-color-based chlorophyll-a are limited [21]. Due to spectral separation issues caused by foam, floating plants, or debris in the mucilage, shadowing and glare must be accounted for [22]. A study using PRISMA data in the Sea of Marmara enabled discrimination among mucilage types; white, yellow, and brown were distinguished, and independent mapping was achieved [23].

Spectral indices and floating-biomass data are widely used for mucilage detection. Phytoplankton detection can be achieved by using contrast with indicators such as the Normalized Difference Chlorophyll Index (NDCI) [24], Floating Algae Index (FAI) [25], and Maximum Chlorophyll Index (MCI) [26]. Because the correlation between chlorophyll-a alone and mucilage detection is weak, index-based approaches need to be supported with multiple data sets and a spatially based support due to the inherent risk of generating inaccurate data [22].

The sensors and other detection products also impose physical limitations. The spectral properties of Sentinel-2 MSI and Landsat OLI can increase the success rate in complex waters such as the Sea of Marmara [27]. However, atmospheric movements, sunlight, and cloud effects can create uncertainties in coastal areas. Various correction approaches exist for this purpose [28].

In recent years, deep learning and computer vision methods have become widespread for detecting mucilage. Deep learning classification and object detection methods can be used for remote detection of mucilage [29]. In addition, there are also studies on segmentation [30]. For segmentation, architectures such as U-Net [29] and DeepLabv3+ [31] enable the capture of small and irregular shapes at the pixel level. In object detection, YOLO [12] and DETR [32] methods provide dynamic structures for temporal data.

Deep learning applications generally employ a hybrid workflow that combines an index-based preprocessing stage with a region-detection stage. This method reduces misleading

information, such as foam, marine litter, or breaking wave crests, when detecting mucilage, and facilitates learning. Pixel-level verification is particularly common in applications using U-Net and DeepLab [33].

The lack of a definitive criterion for the status of mucilage over time and changing conditions creates the problem of labeled data. To overcome this problem, data augmentation [34], pre-training with semi-supervised learning, pseudo-labeling [35], and transfer learning methods are used. These methods can address the challenges of class imbalance between water and mucilage, as well as the variety in appearance across color and phase.

3 MATERIALS AND METHODS

3.1 Dataset

This study used the dataset developed by Yurdakul, which focuses on object detection and includes 1113 images labeled with delimiters from satellite imagery showing mucilage formations [36]. The images in the dataset were obtained from Sentinel-2 and similar sources. Labeling was based on a single class based on the presence of mucilage. Areas where mucilage is found are marked with boxes in the dataset. These boxes support pixelation for segmentation studies. The dataset contains images of different resolutions. The scale was scaled to 768*768 for training.

The dataset aims to ensure the discrimination of mucilage in scenes containing single-class but complex features. Complexities such as sea surface color, foam, waves, sun reflection, and proximity to the shore pose limitations for mucilage detection. The standard metrics mAP@0.5 and mAP@0.5:0.95 were used to evaluate the dataset. The box labels for mucilage detection were created to cover the entire target. In cases where multiple mucilages were present in a single image, the multi-box method was applied. 85% of the dataset was allocated to training, 13% to validation, and 2% to testing. Limitations of the dataset include the presence of only mucilage labels, low mucilage contrast in some images, and reliance on human labeling. However, various augmentation techniques were used to address these limitations. These techniques included mosaics, color space transformation, horizontal flip, random cropping, and random rotation. The dataset, which initially consisted of 1113 images, was enriched by a factor of 5, increasing the total to 5565.

Figure 1. A sample mucilage image from the dataset

Figure 1 presents a sample image from the dataset. A colored frame surrounds mucilage on the sea surface. The image presented in this section is highly distinctive. Mucilage on the sea surface can be detected with minimal loss in this image. However, some factors affecting performance include short-wave crests or foam.

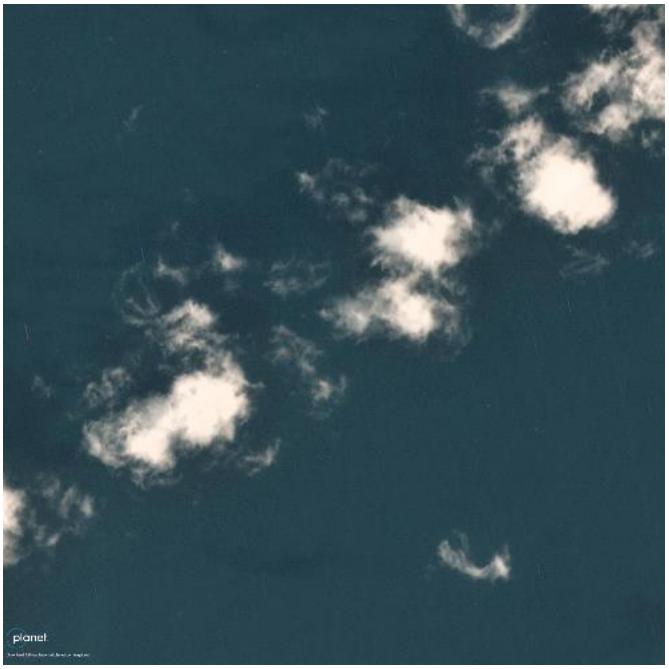

Figure 2. An example of the separation of mucilage from the cloud

Because mucilage resembles a cloud in appearance, an unlabeled cloud image was included in the training process to prevent erroneously detecting similar photos in satellite imagery. An example of an image included in the training is shown in Figure 2. This image enabled the model to recognize cloud structure and reduced false-positive results.

Figure 3. A narrowly defined example of mucilage

Mucilage can be challenging to detect when it hasn't spread over a wide area. Training was supported by images of mucilage flowing in a narrow channel, as shown in Figure 3, to increase success rates.

Figure 4. Example of data near the coastline and without mucilage

In some images where mucilage is absent, identifying the coastline and areas within these strips as mucilage would reduce the success rate. For this reason, in the pictures exemplified in Figure 4, the land connection was identified, and the areas within were not labeled as mucilage.

3.2 Models

In this study, three different model families were chosen for mucilage detection. The YOLO series was used in four different versions. The YOLO architecture was selected for its high success rate and speed-accuracy balance. In contrast, the RF-DETR architecture was chosen for its use of an attention mechanism, its ability to handle complex sea surface images, and the ease of Roboflow labeling, which converts image data into working models.

3.2.1 YOLO

You Only Look Once (YOLO) is a model that uses a single-stage detector for object detection, solving the task using position regression. It has provided significant advantages in speed and accuracy for computer vision. Its first versions, YOLOv1-v3, simplified the pipeline compared to the two-stage R-CNN, enabling real-time operation. The YOLOv4 version introduced a bag-of-freebies approach that supports training [12]. This change enabled the efficiency of backbone-neck-head designs in the subsequent versions, YOLOv7, YOLOv8, YOLOv11, and YOLOv12 [37], [38], [39], [40]. With these changes, it became usable for many more tasks such as object detection, segmentation, and classification. The YOLO model generally uses the mAP@[.50:95] metric. In this study, the study was evaluated using two different metrics. When YOLOv7 was released, it achieved better speed and accuracy than the state of the art in the literature. YOLOv8, YOLOv11, and YOLOv12 offered advantages, including task diversity and ease of distribution.

3.2.2 ResNet-Free Detection Transformer (RF-DETR)

ResNet-Free Detection Transformer (RF-DETR) is a deep learning model used in object detection. RF-DETR is a transformer-based structure that adapts the DETR model [41] formulation to real-time conditions. The RF-DETR model is a continuation of the Detection Transformer (DETR) architecture, which eliminates the complexity inherent in traditional methods, transforming object detection into a single-stage, end-to-end problem. Unlike traditional object detection models, this model does not use a CNN architecture such as ResNet [14]. This simplifies the model's architecture but significantly reduces computational requirements. This results in a lighter, faster, and more efficient model.

RF-DETR uses the transformer's attention mechanism to acquire information from image pixels. This allows the model to directly predict object locations and classes in the image using multiple queries. This structure eliminates the need for predefined fixed anchor boxes.

RF-DETR boasts architectural flexibility, allowing it to adapt to images of varying resolutions. Because the model doesn't use the ResNet framework, both training and inference processes are accelerated. This provides advantages for resource-constrained platforms such as mobile devices, real-time image processing, and autonomous vehicles.

3.2.3 RoboFlow 3.0

RoboFlow is a platform used for dataset management and automation in computer vision projects. New features, particularly in version 3.0, have been added to simplify and accelerate the workflow when working with large datasets. RoboFlow's primary mission is to automate the conversion of image data into formats that are understandable to machine learning or deep learning models. [42].

One of RoboFlow's most important features is its automatic labeling. Manual labeling of a large dataset is time-consuming and costly. This platform allows users to label objects, keypoints, or segmentation masks in an image using pre-trained models or their own model. This step is crucial for data augmentation and various preprocessing operations on the dataset. [43]. RoboFlow offers a range of preprocessing and augmentation options. It can perform operations such as cropping, resizing, rotating, and color changes on images to achieve data augmentation.

3.3 Evaluation Metrics

To evaluate model performance, the Precision, Recall, and mAP metrics, which are standard in computer vision, were used. The metrics take values between 0 and 1; values closer to 1 indicate high model success.

$$Precision = \frac{TP}{TP + FP} \tag{1}$$

The formula for the Precision metric is given in Equation 1. Precision indicates how many of the model's mucilage classifications actually contain mucilage. Precision uses True Positive (TP) and False Positive (FP) values. True Positive (TP) denotes the image regions in which the model correctly detects mucilage. In contrast, False Positive (FP) images are classified as mucilage by the model even though they do not contain mucilage. A high Precision value indicates that the model has a low false classification rate and that False Positive predictions are minimized.

$$Recall = \frac{TP}{TP + FN} \tag{2}$$

The formula for the Recall metric is presented in Equation 2. Recall represents the percentage of the image containing mucilage that the model correctly detected. Similar to the Precision metric, True Positive (TP) denotes image regions in which the model correctly detected mucilage. In contrast, False Positive (FP) denotes images classified as mucilage by the model that do not actually contain mucilage. A high Recall value indicates a low rate of missed areas containing mucilage.

mAP (Mean Average Precision): The average precision computed across different IoU (Intersection over Union) thresholds. mAP@0.5 represents the case where the IoU threshold is 0.50; mAP@0.5:0.95 means the average of the cases where the IoU threshold is increased from 0.50 to 0.95 in 0.05 increments. A higher mAP@0.5:0.95 metric indicates that the model draws the object boundaries (bounding box) much more precisely.

4 RESULTS AND DISCUSSION

In this study, six deep learning models were implemented to detect mucilage using satellite imagery. The studies were conducted in the Google Colab Pro environment using an NVIDIA Tesla T4 (16 GB VRAM) for the GPU, an Intel Xeon @ 2.20 GHz (2 cores) for the CPU, and 12 GB of RAM. The Randomized Search method was used to find the optimal hyperparameter values during model training. This method optimized critical parameters, including learning_rate, imgsz, and batch size. For example, the initial image size was increased from 640 to 768, the batch size from 8 to 16, and the number of epochs from 50 to 80. The performance of six different models was examined in detail. Each model was trained on the optimized dataset and then tested. The models' performance was compared using the precision, recall, mAP@0.5, and mAP@0.5:0.95 metrics.

Table 1. Hyperparameter values before and after optimization

Hyperparameter	Starting Value	Optimized Value
imgsz	640	768
batch size	8	16
epochs	50	80
learning rate	0.01	0.003

Table 1 presents the hyperparameter values that were changed during the optimization process. The hyperparameter optimization process is implemented to maximize model performance. The goal is to improve the results obtained with the initially determined

hyperparameters by adjusting them to achieve higher metric values. The optimization process has increased the success rate. During optimization, the image size, controlled by the imgsz hyperparameter, was increased from 640 to 768. The larger image size allows the model to process more pixel information, enabling it to distinguish mucilage more effectively, which is difficult to detect due to its small size. The batch size value was increased from 8 to 16. A larger value speeds up the training process and yields more accurate weight updates by stabilizing the model's learning. The Epoch hyperparameter was increased from 50 to 80. This increase allows the models to view the dataset more times and learn its features in depth. This increase in the number of epochs also introduces the risk of overfitting. Therefore, the learning rate hyperparameter was lowered from 0.01 to 0.003. A lower learning rate allows the model to identify the conditions that yield the best performance more accurately.

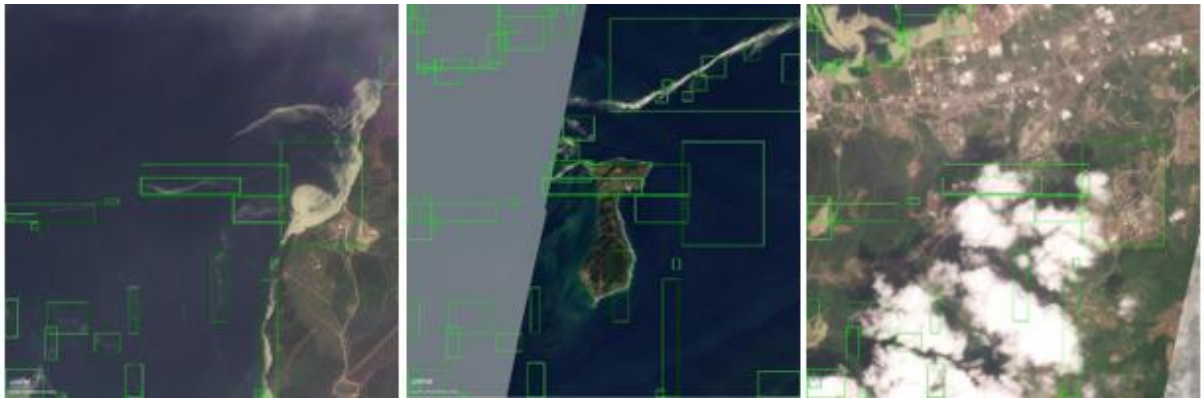

Figure 5. YOLOv7 test images

Figure 5 shows three different test images obtained with the YOLOv7 model. This model successfully detected large areas of mucilage along with some small, scattered fragments. Mucilage detected in green boxes indicates the model's high recall performance. However, the model made an error by identifying some cloud regions and white areas along the coastline as mucilage. This results in a decrease in precision.

Figure 6. YOLOv8 test images

Figure 6 shows three different images obtained during the testing phase of the YOLOv8 model. The model clearly and accurately delineated mucilage areas. It detected both large and delicate structures within the mucilage areas. These detected areas enable the model to achieve high precision and recall values. The model's success rate was increased by highlighting fewer areas, such as clouds and coastlines.

Figure 7. YOLOv11 test images

Figure 7 shows three test images of the YOLOv11 model. While the model correctly identified some prominent mucilage areas, it failed to capture fine and scattered mucilage structures. The model generally focused on highly prominent, dense regions of mucilage. This resulted in a decrease in the model's recall performance. However, a high accuracy rate was observed for the detected points.

Figure 8. YOLOv12 test images

Figure 8 shows three examples of images obtained after testing with the YOLOv12 model. The model attempted to detect mucilage on a large scale. It was remarkably effective at detecting areas of mucilage near the coastline and in open-sea areas. However, excessive limiting factors in some areas resulted in low model precision.

Figure 9. RF-DETR test images

Figure 9 shows three different images obtained during the testing of the RF-DETR model. While the model was successful at detecting large, distinct mucilage areas, it generated fewer boxes than other YOLO models. In this case, fewer mucilage areas were detected, with small, scattered patches. This resulted in a significant decrease in recall performance.

Figure 10. RoboFlow 3.0 test images

Figure 10 shows three test images obtained with the RoboFlow 3.0 model. The model has lower detection potential than other models. While it detected some mucilage regions, it failed to capture many of the areas identified by different models. The model's limited bounding box suggests low recall and an inability to detect objects in certain situations.

Table 2. Model performance comparison

Model	Precision	Recall	mAP@0.5	mAP@0.5:0.95
YOLOv7	0.56	0.51	0.52	0.29
YOLOv8	0.59	0.47	0.54	0.33
YOLOv11	0.58	0.45	0.48	0.26
YOLOv12	0.58	0.45	0.48	0.29
RF-DETR	0.57	0.44	0.49	0.29
Roboflow 3.0	0.55	0.40	0.41	0.29

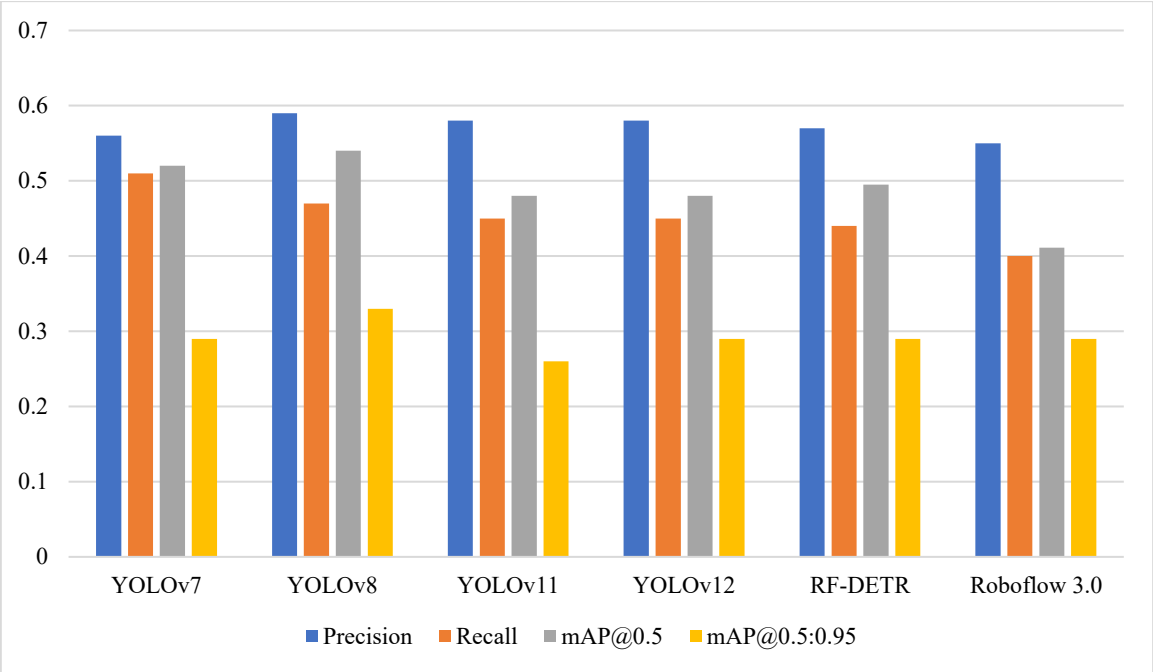

Figure 11. Comparative analysis graph of models with four different metrics

Table 2 and Figure 11 present the performance of six different models across four different metrics. Analysis was conducted using the precision, recall, mAP@0.5, and mAP@0.5:0.95 metrics. These metrics enable a detailed comparison of the models' predictive accuracy and coverage.

According to the results, the YOLOv8 model demonstrated the highest performance. The YOLOv8 model achieved the highest values of mAP@0.5 (0.54) and mAP@0.5:0.95 (0.33). The model achieved a more balanced and successful result compared to the other models in terms of precision and recall. The highest performance in the mAP@0.5:0.95 metric demonstrates consistent success across different thresholds. The main reason the YOLOv8 model performs better than other methods, especially in the mAP@0.5:0.95 (0.33) metric, is its advanced anchor-free detection architecture and its compatibility with mosaic data enhancement techniques. The mucilage structures in the dataset are amorphous, scattered, and highly variable in size (thin strips or large masses). While models that operate with fixed query logic, such as RF-DETR, or rely on rigid anchor boxes, like previous YOLO versions, struggle to capture these irregular geometries fully, YOLOv8's flexible architecture has been able to model better the heterogeneous structure of mucilage and its complex relationship with the shoreline. This has increased the model's sensitivity, especially in detecting small and fragmented mucilage structures.

The YOLOv11 and YOLOv12 models approached the YOLOv8 model in precision (0.58), but fell behind in recall and mAP. This result indicates that the YOLOv11 and YOLOv12 models' predictions are more accurate, but they struggle to capture the entire mucilage area in the images.

YOLOv7 achieved the highest recall of 0.51. This result indicates that it can detect a larger portion of the mucilage in the images. However, the low precision value suggests that the model may produce false positive results.

While the RF-DETR model achieved acceptable precision, its recall and mAP are lower than those of the other models. The results indicate that it lags behind the YOLO models.

The RoboFlow 3.0 model performed least accurately in both precision and mAP. The results indicated that it was less suitable than other models for the dataset and problem used in this study.

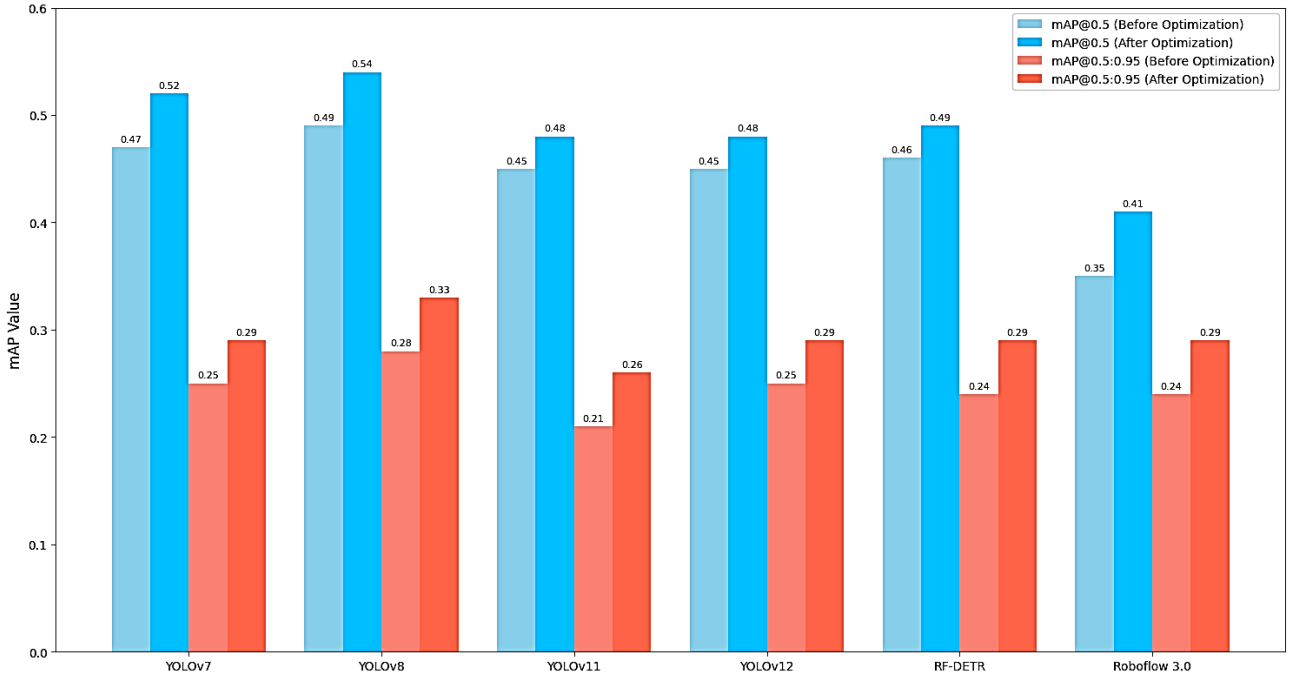

Figure 12. The effect of hyperparameter optimization on mAP performance in models

Figure 12 presents the impact of hyperparameter optimization on model performance for the mAP@0.5 and mAP@0.5:0.95 metrics. Hyperparameter optimization improved performance for all models. Specifically, increases in the mAP@0.5:0.95 metric indicated that a stricter threshold improved the model's ability to detect mucilage areas and was more generalizable, avoiding overfitting.

When the quantitative data and visual results are evaluated together, significant differences are observed in the models' error profiles. The widening gap between mAP@0.5 and mAP@0.5:0.95 values in Table 2 shows that, in general, all models are successful in detecting the presence of mucilage, but struggle to define its boundaries with pixel precision. The amorphous and fluid nature of mucilage is the main factor that makes it difficult to draw precise boundary boxes. A detailed examination of the visual outputs reveals that the RF-DETR and Roboflow 3.0 models are particularly insufficient in detecting thin mucilage strips near the shore, and the 'False Negative' rate increases. In contrast, YOLOv7, despite showing high sensitivity (recall), tends to produce 'False Positives' by occasionally labeling wave foam or shallow coastal areas as mucilage. YOLOv8, with the addition of cloud and negative samples to the training set, emerged as the most stable and robust model in both shoreline differentiation and the overall detection of heterogeneous mucilage particles.

5 CONCLUSION

This study investigated the detection of sea mucilage using images from an open-access satellite dataset. Preprocessing was performed on the dataset, and the data volume was increased by a factor of 5 using various data enhancement techniques. Six object detection models were used: YOLOv7, YOLOv8, YOLOv11, YOLOv12, RF-DETR, and Roboflow 3.0.

The results showed that object detection was difficult due to the irregular, ill-defined structure of the mucilage. Despite this difficulty, YOLO-based architectures proved more successful than other models in detecting heterogeneous and low-contrast structures. This is attributed to the YOLO architecture's multi-scale feature extraction and local pattern sensitivity.

More successful results were achieved in optimizing the models' hyperparameters. The same data was fed into all six models based on the optimization results, and the results were compared. The results showed that the YOLOv8 model achieved the best performance. The YOLOv7 model produced better results, particularly in areas of high visual complexity, such as coastlines, and in detecting fragmented mucilage clusters. It achieved the highest recall, ensuring that large, low-contrast areas were not missed. However, its low precision value indicates a potential for false positives. The RF-DETR and RoboFlow 3.0 models lagged behind the YOLO models. The RF-DETR model showed acceptable precision, but its recall and mAP were lower. RoboFlow 3.0 achieved the lowest precision and mAP. This result indicates that the RoboFlow model is the least suitable for this dataset.

Overall, the results show that the YOLO architecture is a suitable and reliable model for mucilage detection in satellite imagery. The YOLOv8 model was evaluated as the strongest model in this study due to its balance of performance and stability.

6 LIMITATIONS AND FUTURE WORK

The most significant limitation of the study is the dataset's size. While data augmentation techniques have expanded the dataset, the limited availability of images from different geographic areas and seasonal conditions has limited the models' ability to generalize. The relatively low resolution of satellite images has made it difficult to detect small details in mucilage.

Future studies could use images acquired from different satellite sensors at various time intervals to create a larger, more diverse dataset. In the future, semantic segmentation and classification models could be added for comparative analysis.

Conflict of Interest Statement

There is no conflict of interest between the authors.

Statement of Research and Publication Ethics

The study is complied with research and publication ethics.

Artificial Intelligence (AI) Contribution Statement

This manuscript was entirely written, edited, analyzed, and prepared without the assistance of any artificial intelligence (AI) tools. All content, including text, data analysis, and figures, was solely generated by the authors.

Contributions of the Authors

Conceptualization, Y.E.Ç. and E.E.; methodology Y.E.Ç. ve E.E.; validation, E.E. research, Y.E.Ç. and E.E.; references, Y.E.Ç. and E.E.; data editing, Y.E.Ç.; writing-original drafting, Y.E.Ç. ve E.E.; writing-review and editing, E.E.; checking, E.E. All authors have read and accepted the published version of the manuscript.

REFERENCES

[1] C. Totti et al., 'Phytoplankton size-distribution and community structure in relation to mucilage occurrence in the northern Adriatic Sea', Sci. Total Environ., vol. 353, no. 1–3, pp. 204–217, Dec. 2005, doi: 10.1016/j.scitotenv.2005.09.028.

[2] V. Flander-Putrle and A. Malej, 'The evolution and phytoplankton composition of mucilaginous aggregates in the northern Adriatic Sea', *Harmful Algae*, vol. 7, no. 6, pp. 752–761, 2008.

[3] B. Yalçın, M. L. Artüz, A. Pavlidou, S. Çubuk, and M. Dassenakis, 'Nutrient dynamics and eutrophication in the Sea of Marmara: Data from recent oceanographic research', *Sci. Total Environ.*, vol. 601–602, pp. 405–424, Dec. 2017, doi: 10.1016/j.scitotenv.2017.05.179.

[4] V. Turk, Å. Hagström, N. Kovač, and J. Faganeli, 'Composition and function of mucilage macroaggregates in the northern Adriatic', *Aquat. Microb. Ecol.*, vol. 61, no. 3, pp. 279–289, 2010.

[5] A. Ü. Kömüşcü, M. Aksoy, and O. H. Dogan, 'An analysis of meteorological conditions in relation to occurrence of the mucilage outbreaks in Sea of Marmara, March-June 2021', *Int. J. Environ. Geoinformatics*, vol. 9, no. 3, pp. 126–145, 2022.

[6] C. Xie *et al.*, 'Environmental factors influencing mucilage accumulation of the endangered Brasenia schreberi in China', *Sci. Rep.*, vol. 8, no. 1, p. 17955, 2018.

[7] U. Karadurmuş and M. Sari, 'Marine mucilage in the Sea of Marmara and its effects on the marine ecosystem: mass deaths', *Turk. J. Zool.*, vol. 46, no. 1, pp. 93–102, 2022.

[8] D. F. Demirel and E. D. Gönül-Sezer, 'Analyzing the impacts of mucilage in the Sea of Marmara: A system dynamics approach integrating sustainability perspectives', *Ecol. Model.*, vol. 507, p. 111166, 2025.

[9] R. Danovaro *et al.*, 'Implementing and innovating marine monitoring approaches for assessing marine environmental status', *Front. Mar. Sci.*, vol. 3, p. 213, 2016.

[10] P. Cipollini, F. M. Calafat, S. Jevrejeva, A. Melet, and P. Prandi, 'Monitoring sea level in the coastal zone with satellite altimetry and tide gauges', *Integr. Study Mean Sea Level Its Compon.*, pp. 35–59, 2017.

[11] G. Volpe, R. Santoleri, V. Vellucci, M. R. d'Alcalà, S. Marullo, and F. d'Ortenzio, 'The colour of the Mediterranean Sea: Global versus regional bio-optical algorithms evaluation and implication for satellite chlorophyll estimates', *Remote Sens. Environ.*, vol. 107, no. 4, pp. 625–638, 2007.

[12] J. Redmon, S. Divvala, R. Girshick, and A. Farhadi, 'You Only Look Once: Unified, Real-Time Object Detection', May 09, 2016, *arXiv*: arXiv:1506.02640. doi: 10.48550/arXiv.1506.02640.

[13] S. Ren, K. He, R. Girshick, and J. Sun, 'Faster R-CNN: Towards Real-Time Object Detection with Region Proposal Networks', Jan. 06, 2016, *arXiv*: arXiv:1506.01497. doi: 10.48550/arXiv.1506.01497.

[14] R. Sapkota, R. H. Cheppally, A. Sharda, and M. Karkee, 'RF-DETR Object Detection vs YOLOv12 : A Study of Transformer-based and CNN-based Architectures for Single-Class and Multi-Class Greenfruit Detection in Complex Orchard Environments Under Label Ambiguity', Apr. 17, 2025, *arXiv*: arXiv:2504.13099. doi: 10.48550/arXiv.2504.13099.

[15] V. Khryashchev and R. Larionov, 'Wildfire segmentation on satellite images using deep learning', in *2020 Moscow Workshop on Electronic and Networking Technologies (MWENT)*, IEEE, 2020, pp. 1–5.

[16] R. Danovaro, S. Fonda Umani, and A. Pusceddu, 'Climate change and the potential spreading of marine mucilage and microbial pathogens in the Mediterranean Sea', *PloS One*, vol. 4, no. 9, p. e7006, 2009.

[17] N. Balkis, H. Atabay, I. Türetgen, S. Albayrak, H. Balkis, and V. Tüfekçi, 'Role of single-celled organisms in mucilage formation on the shores of Büyükada Island (the Marmara Sea)', *J. Mar. Biol. Assoc. U. K.*, vol. 91, no. 4, pp. 771–781, 2011.

[18] A. L. Yagci, I. Colkesen, T. Kavzoglu, and U. G. Sefercik, 'Daily monitoring of marine mucilage using the MODIS products: a case study of 2021 mucilage bloom in the Sea of Marmara, Turkey', *Environ. Monit. Assess.*, vol. 194, no. 3, p. 170, 2022.

[19] A. Tuzcu Kokal, N. Olgun, and N. Musaoğlu, 'Detection of mucilage phenomenon in the Sea of Marmara by using multi-scale satellite data', *Environ. Monit. Assess.*, vol. 194, no. 8, p. 585, 2022.

[20] C. Hu, 'Sea snots in the Marmara Sea as observed from medium-resolution satellites', *IEEE Geosci. Remote Sens. Lett.*, vol. 19, pp. 1–5, 2022.

[21] C. Hu, L. Qi, Y. Xie, S. Zhang, and B. B. Barnes, 'Spectral characteristics of sea snot reflectance observed from satellites: Implications for remote sensing of marine debris', *Remote Sens. Environ.*, vol. 269, p. 112842, Feb. 2022, doi: 10.1016/j.rse.2021.112842.

[22] K. Kikaki, I. Kakogeorgiou, I. Hoteit, and K. Karantzalos, 'Detecting Marine pollutants and Sea Surface features with Deep learning in Sentinel-2 imagery', *ISPRS J. Photogramm. Remote Sens.*, vol. 210, pp. 39–54, Apr. 2024, doi: 10.1016/j.isprsjprs.2024.02.017.

[23] K. G. Toker and S. E. Yuksel, 'Multi-scale superpixel-based nearest subspace classifier for mucilage detection from hyperspectral PRISMA data', *Digit. Signal Process.*, vol. 154, p. 104657, Nov. 2024, doi: 10.1016/j.dsp.2024.104657.

[24] S. Mishra and D. R. Mishra, 'Normalized difference chlorophyll index: A novel model for remote estimation of chlorophyll-*a* concentration in turbid productive waters', *Remote Sens. Environ.*, vol. 117, pp. 394–406, Feb. 2012, doi: 10.1016/j.rse.2011.10.016.

[25] C. Hu, 'A novel ocean color index to detect floating algae in the global oceans', *Remote Sens. Environ.*, vol. 113, no. 10, pp. 2118–2129, Oct. 2009, doi: 10.1016/j.rse.2009.05.012.

[26] C. E. Binding, T. A. Greenberg, and R. P. Bukata, 'The MERIS Maximum Chlorophyll Index; its merits and limitations for inland water algal bloom monitoring', *J. Gt. Lakes Res.*, vol. 39, pp. 100–107, Jan. 2013, doi: 10.1016/j.jglr.2013.04.005.

[27] M. Drusch *et al.*, 'Sentinel-2: ESA's Optical High-Resolution Mission for GMES Operational Services', *Remote Sens. Environ.*, vol. 120, pp. 25–36, May 2012, doi: 10.1016/j.rse.2011.11.026.

[28] S. Kay, J. D. Hedley, and S. Lavender, 'Sun Glint Correction of High and Low Spatial Resolution Images of Aquatic Scenes: a Review of Methods for Visible and Near-Infrared Wavelengths', *Remote Sens.*, vol. 1, no. 4, pp. 697–730, Oct. 2009, doi: 10.3390/rs1040697.

[29] X. X. Zhu *et al.*, 'Deep Learning in Remote Sensing: A Comprehensive Review and List of Resources', *IEEE Geosci. Remote Sens. Mag.*, vol. 5, no. 4, pp. 8–36, Dec. 2017, doi: 10.1109/MGRS.2017.2762307.

[30] G. Cheng, J. Han, and X. Lu, 'Remote Sensing Image Scene Classification: Benchmark and State of the Art', *Proc. IEEE*, vol. 105, no. 10, pp. 1865–1883, Oct. 2017, doi: 10.1109/JPROC.2017.2675998.

[31] L.-C. Chen, Y. Zhu, G. Papandreou, F. Schroff, and H. Adam, 'Encoder-Decoder with Atrous Separable Convolution for Semantic Image Segmentation', presented at the Proceedings of the European Conference on Computer Vision (ECCV), 2018, pp. 801–818. Accessed: Aug. 26, 2025. [Online]. Available: https://openaccess.thecvf.com/content_ECCV_2018/html/Liang-Chieh_Chen_Encoder-Decoder_with_Atrous_ECCV_2018_paper.html

[32] N. Carion, F. Massa, G. Synnaeve, N. Usunier, A. Kirillov, and S. Zagoruyko, 'End-to-End Object Detection with Transformers', May 28, 2020, *arXiv*: arXiv:2005.12872. doi: 10.48550/arXiv.2005.12872.

[33] I. Colkesen, T. Kavzoglu, U. G. Sefercik, and M. Y. Ozturk, 'Automated mucilage extraction index (AMEI): a novel spectral water index for identifying marine mucilage formations from Sentinel-2 imagery', *Int. J. Remote Sens.*, vol. 44, no. 1, pp. 105–141, 2023, doi: 10.1080/01431161.2022.2158049.

[34] C. Shorten and T. M. Khoshgoftaar, 'A survey on Image Data Augmentation for Deep Learning', *J. Big Data*, vol. 6, no. 1, p. 60, Jul. 2019, doi: 10.1186/s40537-019-0197-0.

[35] M. Leenstra, D. Marcos, F. Bovolo, and D. Tuia, 'Self-supervised pre-training enhances change detection in Sentinel-2 imagery', Apr. 11, 2021, *arXiv*: arXiv:2101.08122. doi: 10.48550/arXiv.2101.08122.

[36] M. Yurdakul, 'Mucilage Dataset', *Roboflow Universe*. Roboflow, Dec. 2023. [Online]. Available: https://universe.roboflow.com/mustafa-yurdakul/mucilage-bftvt

[37] C.-Y. Wang, A. Bochkovskiy, and H.-Y. M. Liao, 'YOLOv7: Trainable Bag-of-Freebies Sets New State-of-the-Art for Real-Time Object Detectors', in *2023 IEEE/CVF Conference on Computer Vision and Pattern Recognition (CVPR)*, Vancouver, BC, Canada: IEEE, Jun. 2023, pp. 7464–7475. doi: 10.1109/CVPR52729.2023.00721.

[38] M. Sohan, T. Ram, and V. Ch, 'A Review on YOLOv8 and Its Advancements', 2024, pp. 529–545. doi: 10.1007/978-981-99-7962-2_39.

[39] R. Khanam and M. Hussain, 'YOLOv11: An Overview of the Key Architectural Enhancements', Oct. 23, 2024, *arXiv*: arXiv:2410.17725. doi: 10.48550/arXiv.2410.17725.

[40] Y. Tian, Q. Ye, and D. Doermann, 'YOLOv12: Attention-Centric Real-Time Object Detectors', Feb. 18, 2025, *arXiv*: arXiv:2502.12524. doi: 10.48550/arXiv.2502.12524.

[41] N. Carion, F. Massa, G. Synnaeve, N. Usunier, A. Kirillov, and S. Zagoruyko, 'End-to-End Object Detection with Transformers', May 28, 2020, *arXiv*: arXiv:2005.12872. doi: 10.48550/arXiv.2005.12872.

[42] S. Alexandrova, Z. Tatlock, and M. Cakmak, 'RoboFlow: A flow-based visual programming language for mobile manipulation tasks', in *2015 IEEE International Conference on Robotics and Automation (ICRA)*, May 2015, pp. 5537–5544. doi: 10.1109/ICRA.2015.7139973.

[43] C. Sager, C. Janiesch, and P. Zschech, 'A survey of image labelling for computer vision applications', *J. Bus. Anal.*, vol. 4, no. 2, pp. 91–110, Jul. 2021, doi: 10.1080/2573234X.2021.1908861.